Field Ion Emission in an Atom Probe Microscope Triggered by Femtosecond-Pulsed Coherent Extreme Ultraviolet Light‡

Short Title: Field Ion Emission using Extreme Ultraviolet Light

Ann N. Chiaramonti[1]*, Luis Miaja-Avila[2], Benjamin W. Caplins[1], Paul T. Blanchard[2], David R. Diercks[3], Brian P. Gorman[3], and Norman A. Sanford[2].

[1] *Material Measurement Laboratory, National Institute of Standards and Technology, Boulder, CO 80305, USA*

[2] *Physical Measurement Laboratory, National Institute of Standards and Technology, Boulder, CO 80305, USA*

[3] *Colorado School of Mines, Department of Metallurgical and Materials Engineering, Golden, CO 80401, USA*

* Corresponding author.

325 Broadway St., Mailstop 647. Boulder, CO 80305

Phone: +01 303 497 5701

Fax: +01 303 497 xxxx

Email: chiaramonti@nist.gov

Abstract

This paper describes initial experimental results from an extreme ultraviolet (EUV) radiation-pulsed atom probe microscope. Femtosecond-pulsed coherent extreme ultraviolet radiation of 29.6 nm wavelength (41.85 eV photon energy), obtained through high harmonic generation in an Ar-filled hollow capillary waveguide, successfully triggers controlled field ion emission from the apex of amorphous SiO_2 specimens. The calculated composition is stoichiometric within the error of the measurement and effectively invariant of the specimen base temperature in the range 25 K to 150 K. Photon energies available in the EUV band are significantly higher than those currently used in state-of-the-art near ultraviolet laser-pulsed atom probe, which enables the possibility of additional ionization and desorption pathways. Pulsed coherent EUV light is a new and potential alternative to near-ultraviolet radiation for atom probe tomography.

Key words: atom probe tomography, field ion emission, EUV, femtosecond pulse

Introduction

In modern three-dimensional (3D) laser-pulsed atom probe tomography (APT), a pulsed laser (typically near ultraviolet (NUV); 300 nm ≤ λ ≤ 400 nm (ISO-21348, 2013)) incident on an electrically biased, needle-shaped specimen provides a thermal transient to overcome the activation energy barrier to field ion evaporation (Kellogg, 1987; Kelly & Miller, 2007; Gault et al., 2012; Larson et al., 2013; Kelly et al., 2014; Miller & Forbes, 2014; Lefebvre-Ulrikson et al., 2016). In addition to metallic specimens, which are highly absorbing in the NUV band, NUV laser-pulsed 3D APT (hereafter simply referred to as NUV APT) is also routinely used on materials that weakly absorb or are essentially transparent at those wavelengths in the bulk. For example, SiO_2,

diamond, yttria-stabilized zirconia, Al_2O_3, and MgO have optical bandgaps above the typical NUV photon energy of ≈ 3.5 eV, but have been successfully examined in the bulk using laser-pulsed APT (Larson et al., 2008; Schirhagl et al., 2015; Ohkubo et al., 2009; Marquis et al., 2010; Stiller et al., 2013). The mechanism of high-field sub-gap photon absorption as it pertains to NUV APT may vary depending on the material and experimental conditions. Several schemes have been proposed (Marquis et al., 2010; Chen et al., 2011; Mazumder et al., 2010; Silaeva et al., 2013, 2014; Vella, 2013), e.g. photo-generated holes at the sample surface, band bending and metal-like behavior resulting from the high applied field, Franz-Keldysh effects, multi-photon effects, or gap states introduced by vacancies, interstitials, or surface amorphization from the sample preparation process itself.

Following the successful initial demonstration of photon-stimulated field ionization using a 300 nm dye laser in 1976 (Tsong et al., 1976), the pulsed-laser imaging atom probe instrument developed by Kellogg and Tsong in 1980 (Kellogg & Tsong, 1980; Tsong et al., 1982) employed a 337 nm nitrogen laser and demonstrated photon-assisted field ion evaporation of both metals and semiconductors. The first commercial laser-pulsed atom probe field ion microscope (Cerezo et al., 1984) followed in 1984 and used 532 nm light from a frequency doubled Nd:YAG system. Throughout the late 1980s and 1990s further developments in laser-pulsed APT slowed due to the difficulty and expense involved in integrating the unreliable pulsed laser technology available at the time (Gault et al., 2006; Bunton et al., 2007; Kelly & Miller, 2007; Lefebvre-Ulrikson et al., 2016). However, in the early 2000s both pulsed laser and 3D atom probe technology and hardware improved to a point that several groups renewed the idea of photon-assisted field ion evaporation for 3D APT (Deconihout et al., 2004; Gault et al., 2006; Cerezo et al., 2006; Bunton et al., 2007).

Early modern laser-pulsed 3D APT instruments used lasers with fundamental wavelengths in the infrared (IR; ranging from λ = 1064 nm down to λ = 780 nm); these subsequently evolved over time to use frequency doubled visible (λ = 532 nm or λ = 515 nm) and now frequency tripled (or even quadrupled) NUV and mid-ultraviolet wavelengths (λ = 355 nm to λ = 258 nm) (Renaud et al., 2006; Cerezo et al., 2006; Gault et al., 2006; Bunton et al., 2007; Deconihout et al., 2007; Stender et al., 2007; Vurpillot et al., 2009; Houard et al., 2010; Bunton et al., 2010; Schlesiger et al., 2010; Hono et al., 2011). Each of these changes was a logical progression driven by the observation that APT data quality improved as laser wavelength decreased (Santhanagopalan et al., 2015; Hono et al., 2011; Gault et al., 2011) due to both increased absorption and a concomitant shallower absorption depth, which leads to faster cooling. Such improvements include increasingly narrower peaks/higher mass resolution, the ability to analyze a much larger class of materials including wide band gap semiconductors and insulators, and improved spatial resolution.

Although NUV APT is generally effective for analyzing many materials, numerous artifacts can lead to quantitative compositional errors in the resulting mass spectrum. Such artifacts include peak broadening, peak splitting, and persistent evaporation (in the form of so-called “thermal tails”) (Kelly et al., 2014; Miller et al., 2012; Johnson et al., 2013; Larson et al., 2013; Lefebvre-Ulrikson et al., 2016). The origin of many of these sources of error lies in the fact that laser-pulsing of field evaporation is a thermally-activated process (Kelly et al., 2014; Tsong, 1984; Cerezo et al., 2006; Bunton et al., 2007; Vurpillot et al., 2009; Houard et al., 2010). In laser-pulsed APT, peak broadening and thermal tails arise from persistent or delayed evaporation as the specimen volume remains at elevated temperature and continues to emit ions after the laser pulse has passed. Peak splitting can occur when more than one cooling mechanism is operating simultaneously (Vella et

al., 2011). Artifacts from the thermal process can also be found in the form of increased propensity for molecular cluster ion evaporation, which can lead to degraded spatial resolution (Blum et al., 2016), isobaric overlaps in the mass spectrum, increased multiple hits, or the formation of undetected neutral species from in-flight cluster ion dissociation (Gault et al., 2016).

Therefore, given the persistent and still numerous sources of thermal artifacts in NUV laser-pulsed APT mass spectral data, there is incentive to explore even shorter wavelengths such as those in the extreme ultraviolet (EUV; λ=124 nm to 12 nm, E_{photon}=10 eV to 100 eV) (ISO-21348, 2013). Unlike in the visible or NUV bands, absorption would be virtually assured in nearly any material and within a very shallow depth (Gullikson, 2009). Since the EUV photon energy could be chosen to exceed the bandgap or optical absorption edge of the material to be analyzed, it would be directly absorbed at the surface without any requirement of surface defects, band bending, Franz-Keldysh effects, multi-photon effects, or hole generation. In addition to the possibility of thermal pulsing leading to field evaporation, the much higher photon energies available in the EUV band may more readily promote ionization and desorption pathways that are not routinely observed in NUV APT, involving interband transitions, resonant excitations, and charge transfer via tunneling (Tsong et al., 1976; Tsong, 1978, 1984; Tsong & Kinkus, 1984; Kellogg, 1987; Menand & Kingham, 1985; Nishigaki et al., 1979; Menand et al., 1984). Most significantly and uniquely, since the EUV photon energy can be chosen so that it is above the ionization potential of any element, there are additional athermal ionization mechanisms that are simply not available for most materials when using NUV wavelengths. These include, for example, direct photoionization (defined here as ionization through ejection of a “free” photoelectron above the vacuum level), impact ionization, or ionization through Auger core-hole decay (Knotek & Feibelman, 1978; Knotek et al., 1979).

For metals, surface ions created through athermal processes are expected to be rapidly neutralized by conduction band electrons before desorption can occur (Tsong et al., 1976; Viswanathan et al., 1979; Tsong, 1984; Lichtman & Shapira, 1978). Therefore, athermal ionization mechanisms would most likely be operative in materials with longer surface ion lifetimes, such as semiconductors and insulators.

Picosecond-pulsed EUV radiation from a synchrotron source has been used to study photon-assisted field ionization, photon-assisted field desorption, and field-assisted photodesorption (also known as field-assisted photon stimulated desorption) of various adsorbed gas species on or above a field emitter surface (Weigmann et al., 1984; Drachsel et al., 1985; Jaenicke et al., 1986; Weigmann et al., 1986; Drachsel et al., 1987; Jaenicke et al., 1987; Jaenicke, Ciszewski, Dosselmann, Drachsel, J. Block, et al., 1988; Jaenicke, Ciszewski, Dosselmann, Drachsel, J.H. Block, et al., 1988). Collectively, for photon energies in the EUV band, ionization is attributed to "direct particle-particle interactions" or "quantum excitation" processes, i.e. athermal ionization mechanisms. There is no evidence in previous studies of EUV photon-assisted field evaporation or field-assisted photodesorption *of the substrate atoms themselves*, which is a requirement to perform atom probe tomography. In this paper, we describe the first reported EUV radiation-pulsed atom probe microscope and demonstrate pulsed EUV radiation-assisted field ion emission of substrate atoms in amorphous SiO_2 specimens.

Materials and Methods

Specimens

APT specimens were made from a GE124 fused quartz (amorphous SiO_2) sample (Ted Pella, Redding, CA)[†] and prepared by focused ion beam (FIB) wedge lift-out techniques (Thompson et al., 2007; Miller et al., 2007; Prosa & Larson, 2017). Extracted pieces of the sample material were attached to the posts of Si TEM half-grids (Dune Sciences, Eugene, OR) and sharpened into a needle-like shape by FIB annular milling. The specimens were shaped such that the apex of the needle was at least 50 μm above the substrate. The needle height was selected in order to avoid spurious EUV-induced ion emission from blade edges lower down the shank and to account for the large physical EUV spot size of ≈ 50 μm at the specimen location.

Instrument

The EUV atom probe instrument (Figure 1), described in detail elsewhere (Chiaramonti et al., 2019), consists of a LEAP 3000X-Si (CAMECA Instruments, Madison, WI) straight flight path local electrode atom probe microscope interfaced to a XUUS coherent EUV source (KM Labs, Boulder, CO) driven by a Wyvern (KM Labs, Boulder, CO) ultrafast Ti:sapphire laser by means of a vacuum manifold designed in-house. Briefly, the EUV photons are generated as follows: the Ti:sapphire driving laser produces 35 fs, 1.2 mJ pulses at a repetition rate of 10 kHz and a center wavelength of ≈ 800 nm. A fraction of these pulses (500 μJ) are coaxially focused into an Ar-filled hollow capillary waveguide and drive high harmonic generation (HHG) of the gas medium

[†] Commercial equipment, instruments, or materials are identified only in order to adequately specify certain procedures. In no case does such identification imply recommendation or endorsement by the National Institute of Standards and Technology, nor does it imply that the products identified are necessarily the best available for the purpose.

155 via nonlinear interactions that have been described at length elsewhere (Rundquist et al., 1998). In
156 our system, the EUV pulse width is assumed to be less than 10 femtoseconds based on the
157 measured output of similarly configured systems (Miaja-Avila et al., 2006). As EUV light is
158 attenuated in air, the EUV beam path is necessarily under vacuum. Most of the co-propagating 800
159 nm driving laser light is removed using two "rejector" optics fabricated from Si wafers mounted
160 at approximately Brewster's angle for the driving laser wavelength. Two normal incidence
161 multilayer mirrors mounted on piezoelectric linear actuator motors set up in a "Z" configuration
162 are used to focus and steer the EUV light into the analysis chamber of the atom probe. Multilayer
163 mirror optics work on the principle of interference and act as a band pass filter. As such, the
164 multilayer mirrors were designed to pass a high intensity harmonic with high efficiency. In this
165 case, the central peak for the reflectivity curve of the multilayer mirrors is at 41.85 eV (29.6 nm;
166 the 27th harmonic of the fundamental), with a bandwidth of approximately 2.4 eV. A thin Al filter
167 (200 nm) removes any residual co-propagating 800 nm light before the EUV beam enters the APT
168 analysis chamber. The EUV light is polarized parallel to the long axis of the needle-shaped
169 specimen and was not varied. The EUV pulse energy is 0.5 pJ and was measured at the entrance
170 to the APT analysis chamber using an EUV-sensitive photodiode. The trigger signal for the time
171 of flight (TOF) measurement is from a fast photodiode placed inside the amplifier laser.
172

173 **Data Collection and Analysis**

174 Table 1 details the acquisition parameters for the data presented here. The APT specimen base
175 temperatures were varied between 25 K and 150 K at set point values of 25 K, 50 K, 125 K, and
176 150 K. The pressure in the analytical chamber varied with the specimen base temperature and
177 ranged from ≈ $6x10^{-9}$ Pa ($5x10^{-11}$ Torr) at 25 K to ≈ $1x10^{-8}$ Pa ($1x10^{-10}$ Torr) at 150 K. For the data

shown here, two different specimens were used, however, this data is representative of multiple experiments conducted on many different samples. Specimen A was used for the 25 K and 150 K experiments and Specimen B was used for the 50 K and 125 K experiments. Data were collected at constant voltage, therefore, the evaporation rate was free to fluctuate. The ideal standing voltage was determined for each specimen by *maximizing the apparent evaporation rate of specimen ions,* and was accomplished by monitoring the rate of ^{16}O ion detection. Notably, once the detection rate for specimen ions was maximized, further increases in voltage only increased the time-independent background signal (DC field ionization). The flight path was 90 mm. To facilitate comparison, a subset of each spectrum containing 10^5 counts was taken from the middle of each run and was used to calculate the composition.

Voltage and bowl corrections as well as mass calibration were performed using commercially available atom probe reconstruction and analysis software (CAMECA Instruments IVAS 3.6.10a). Peak ranging, local range-assisted background subtraction, and composition calculations were performed using in-house developed mass spectrum analysis programs (Blanchard et al., 2018) in order to more readily calculate the statistical error as described below. To achieve consistent noise averaging across the mass spectrum, the peak ranging was carried out by first converting the mass-to-charge-state ratio spectrum into an equivalent TOF spectrum, similar to the fictitious time domain described by Johnson et al. (Johnson et al., 2013) The bin width in the TOF spectrum was chosen to be the equivalent of a bin width of 0.005 Da at 20.0 Da in the original mass spectrum. Time-independent background is approximately constant in the TOF domain, at least over the range of mass-to-charge-state-ratio of interest; it is easily identified and subtracted. The local background was estimated using a power law fit to a band of bins preceding the peak. This

is effectively equivalent to the "local range assist" method provided in IVAS. Peak range start and end limits were placed at the locations where the local-background-corrected spectrum count had decreased to less than 10 % of the peak height, where the peak height is defined as the count in the highest-count bin within the range. After finding the peak range limits in the proxy TOF spectrum, those peak range start and end values were converted back into equivalent mass-to-charge-state ratios. In the case of peaks for which the corrected peak height was similar to the noise level, range limits were set manually.

The uncertainty in the global time-independent background is calculated from the standard deviation of the counts in the region of TOF space used. The root mean square (RMS) error of the time-dependent local background fit in the pre-peak region was used as an estimate of the uncertainty in the projected local background in each bin within the peak range. In cases where the RMS error was smaller than the global background uncertainty, the global background uncertainty was used instead. Linear propagation of error (Taylor & Kuyatt, 1994) was used to find the uncertainty in the number of counts in each bin and that error was further propagated to determine the uncertainty in composition. Uncertainty values of 2σ are reported here. Note that the covariance term in the error propagation is non-zero for this composition calculation.

Results

Mass spectra representative of repeated measurements across multiple samples for specimen base temperatures in the range between 25 K and 150 K are shown in Figure 2. Peak assignments in the mass spectra were generally straightforward except for a few ambiguities. Many of the ambiguous assignments have been encountered and discussed in previous studies of SiO_2 (Kellogg, 1982;

Gruber et al., 2009; Duguay et al., 2010; Gilbert et al., 2011; Talbot et al., 2013; Kwak et al., 2017) and other oxides. Based on a combination of measured isotopic ratios, accuracy and plausibility in measured stoichiometry, and consistency when compared with our NUV data and the literature (Bachhav et al., 2013; Kinno et al., 2014), the peak at 16 Da is assigned to $^{16}O^{+}$, the peaks at 17 Da and 18 Da are assigned to chamber-related $^{16}O^{1}H_{n}^{+}$ (and therefore are not included in the composition measurement), and the peak at 32 Da to $^{16}O_{2}^{+}$. The same peak assignments were used for all of the specimens across all of the base temperatures.

The collection of peaks from 28 Da to 29 Da including the small broad peak centered at ~ 28.6 Da do not fit the typically observed isotopic profile of Si^{+} (Figure 3). In fact, the shape and intensity distribution of the peaks in the region between 28 Da and 30 Da inclusive indicate that those peaks most likely contain fractional contributions from Si^{+}, Si_{2}^{++}, and SiO_{2}^{++}, as well as their related hydrides. Similarly, the peaks near 60 Da do not fit the profile of SiO_{2}^{+} alone; they most likely contain contributions from of SiO_{2}^{+}, Si_{2}^{+}, and their related hydrides. Peak decomposition in both of these regions for this data was inconclusive due to the low number of counts contained in those peaks after background subtraction. Of course a stoichiometric result can be obtained using a priori knowledge of the expected composition through peak decomposition and fractional peak assignments, however, this was not considered to be a rigorous method that is well supported by these data. Therefore, to account for this increased uncertainty due to the peak ranging model, two different peak assignments (Table 2) were made in order to cover the widest possible range of oxygen-rich or oxygen-deficient composition that the data could possibly support. Ranging in this manner means that the true measured composition must lie within these bounds. This avoids bias for or against oxygen deficiency or Si hydrides and/or Si dimers. Objectively, there is no information in these mass spectral data that would favor one set of peak assignments over the other.

Composition measured using the two different peak ranging models as a function of the base temperature is enumerated in Table 3. For comparison, we note that composition measurements using the same range files with the local range-assisted background subtraction model embedded in IVAS are within 1σ of those determined using the in-house software.

Discussion

These data establish that EUV photons of $\lambda = 29.6$ nm (E = 41.85 eV) can trigger time-correlated, ion emission of SiO_2 surface atoms in this dielectric material. Further, it demonstrates that there is no obvious trend in the measured oxygen concentration, presence or absence of peaks, or multiple hit counts as a function of the base temperature, particular specimen, standing voltage, or ion detection rate as varied here. There is also not a statistically significant deviation from the expected stoichiometry in the temperature range 25 K to 150 K.

For EUV pulsing, both the time-independent background signal and the signal-to-noise ratio are effectively constant and independent of the base temperature. Independence of ion detection rate as a function of the base temperature has been observed previously in MgO, but only at very high fields (Silaeva et al., 2014). This may be a satisfactory explanation, as the presence of Si^{+++} in the mass spectra indicate that these data were collected in a high field condition. However, the temperature independence of the time-independent background signal (See Figure S1, Supplementary Information) is surprising and unexpected, especially when considering that the background pressure in the chamber increases by nearly an order of magnitude between 25 K and 150 K. This suggests that the time-independent signal is not dominated by DC field evaporation or DC field ionization (these would be thermally activated), nor from ionization of chamber gasses

far from the specimen (rate would be expected to increase with the background pressure, which increases with the base temperature). The source of the athermal noise observed in this EUV data is not yet understood. One possibility is the interaction of the EUV beam with the local electrode or chamber walls, however, further work is required to unambiguously identify the source of the background.

The presence and relative peak heights of the H_n^{x+} species do show a trend with temperature, however this is expected since the formation of H_n^{x+} cluster ions on field emitter surfaces is a temperature-dependent surface chemical reaction (Ernst & Block, 1983). The total H_n^{x+} signal in the EUV data is high. In fact, in the EUV data the H_n^{x+} peak heights are always larger than the specimen ion peak heights. A large H_n^{x+} signal could come from EUV ionization of H along the shank, however, a contribution from the 10 kHz pulse repetition rate or even from the specimen itself cannot be ruled out. For example, if H adsorption is time dependent, a slower repetition rate allows more time for H to absorb and subsequently field evaporate or get directly photolyzed by the EUV light.

The combined effects of the target evaporation rate, temperature, and net surface electric field on the measured oxygen concentration in oxides are complicated and appear to be strongly influenced by the particular material of interest. Depending on e.g. the dielectric constant, thermal conductivity, available valence states for the cation species, and optical absorption of NUV wavelengths, sometimes the experimental parameters can be varied to find a condition which will return the nominal expected oxygen concentration. However, for a great number of other oxide materials, NUV APT will systematically underestimate the nominal oxygen concentration,

295 sometimes no matter how the experiment is performed (Laiginhas et al., 2015; Santhanagopalan
296 et al., 2015; Schreiber et al., 2014; Bachhav et al., 2013; Gin et al., 2013; Mancini et al., 2014;
297 Schreiber et al., 2020). There is a paucity of literature providing systematic study of the effect of
298 base temperature on the measured composition in oxides. The available results show that for some
299 materials such as Al_2O_3, Fe_3O_4, and Fe_2O_3, higher base temperatures lead to higher measured
300 oxygen concentrations (Schreiber et al., 2020; Diercks & Gorman, 2016), whereas for SiO_2, the
301 opposite may be true (Kinno et al., 2014). Note that care must be taken in interpreting the literature
302 for oxides and SiO_2 in particular; indexed mass spectra are not always shown and it is therefore
303 unclear if the peak at 16 Da is assigned to O_2^{++} instead of O^+, which may artificially increase the
304 measured oxygen concentration. What is clear from the available literature, however, is that
305 measured oxygen concentration generally appears to be dependent on the base temperature for
306 oxides. These EUV APT results demonstrate that there is no clear trend in the measured oxygen
307 concentration as a function of the base temperature and that further, the composition as measured
308 by EUV APT is effectively stoichiometric under the various conditions tested here.
309
310 In trying to understand the mechanism of ion emission using pulsed EUV light, it is useful to
311 estimate to a first degree the maximum thermal energy that could possibly be imparted to the
312 specimen from the pulsed EUV beam used in these experiments. Using conservation of energy
313 arguments, the following simple assumptions are made:
314 • The measured pulse energy is 0.5 pJ. The $1/e^2$ beam diameter is 50 μm and has a Gaussian
315 energy distribution. Therefore, the peak EUV fluence (F, energy per unit area) is equal to
316 twice the measured pulse energy divided by the area of the spot $F \approx 5x10^{-8}$ J/cm^2. The
317 factor of two accounts for the assumed Gaussian intensity distribution.

- For this simple calculation diffraction will be ignored. We assume this energy is uniformly distributed and absorbed over spot centered on the specimen tip apex.
- All EUV radiation incident on the model specimen is absorbed and fully thermalized.
- The SiO_2 apex of the specimen needle absorbs the EUV radiation, is a simple rectangle, and measures 100 nm x 100 nm in cross section.

The energy absorbed (E_A) [1] by the cuboidal specimen with cross-sectional area A = $1x10^4$ nm^2 is $5x10^{-3}$ fJ per pulse. This is approximately equal to only one E = 41.85 eV photon incident within 100 nm of the specimen apex *per pulse*. For comparison, in NUV laser pulsing at 300 pJ with a 2 μm spot, there are on the order of 10^6 photons incident on the same area; of course the bulk absorption at that wavelength is significantly less. Applying the above assumptions to the following equation:

$$E_A = F * A \quad [1]$$

the instantaneous temperature rise ΔT [2] is a function of the absorbed energy, the specific heat capacity (c), the density (ρ), and the volume (v) as follows:

$$\Delta T = \frac{E_A}{c\rho v} \qquad [2]$$

At 50 K, the specific heat capacity of SiO_2 is approximately c = 0.1 J/g·K (Gil et al., 1993; Carini et al., 2016). The density of fused silica at cryogenic temperatures is not well reported. However, due to the very low coefficient of thermal expansion (Berthold et al., 1977), it is reasonable to assume the number is very close to the room temperature value of ρ= 2.2 g/cm^3 (Eernisse, 1974). If this energy is relaxed thermally in a 100 nm x 100 nm x 100 nm volume, the temperature rise is approximately equal to 0.02 K; the traditional model of field evaporation by absorption, bulk heating, and thermal cooling could not apply in this case. If the same thermal energy is relaxed in a smaller, nm-sized area localized to only the specimen surface near the apex and measuring 10

nm x 10 nm x 10 nm, then the instantaneous temperature increase could potentially equal ≈ 20 K. Field evaporation might be possible, but only at extremely high electric fields. Thus, in this regime, the classic thermal process of bulk heating is unrealistic. However, if absorption was to occur very close to the specimen surface, and if fast electron-phonon decay was confined to the region close to the site of absorption, then a different, nm-scale absorption-localized heating mechanism might in fact be possible. These two heating models are differentiated here using the terms "bulk heating" and "absorption-localized heating." Therefore, it is difficult to see how EUV APT could proceed through a bulk heating and cooling mechanism as it is currently understood. Further experimentation is required to explore the exact nature of the interaction.

At first it might seem that the very small potential temperature rise may be counter indicated by the fact that the EUV mass spectra of SiO_2 have tails on the high mass side of the peaks that persist over the range of several Da. However, tails in a TOF mass spectrum can arise from a wide variety of mechanisms. The tails present in laser-pulsed APT data are generally attributed to thermal bulk heating and slow cooling mechanisms (Kelly et al., 2014; Tsong, 1984; Cerezo et al., 2006; Bunton et al., 2007; Vurpillot et al., 2009; Houard et al., 2010); thermal tails are formed when the specimen remains at an elevated temperature and continues to evaporate ions for some time following the initial laser pulse. Tails in voltage (field) pulsed APT data are a result of the fact that the voltage is not a perfect square pulse, and the absolute magnitude varies slightly throughout the duration of the pulse. As a result, any ions evaporated at a (slightly) lower voltage are accelerated to a lower kinetic energy than otherwise would be expected, and so have longer flight times. These are known as critical energy deficits (Tsong et al., 1983, 1984; Tsong & Kinkus, 1984). Critical energy deficits can also manifest in the TOF mass spectra of insulators due to charging (Arnoldi et al.,

364 2014), which results in an effective net decrease of the applied voltage at the specimen apex.
365 Similar to the energy deficits seen in voltage pulsing, the ions evaporated when charging is present
366 will be accelerated with a lower kinetic energy than would be expected from the applied voltage
367 alone, leading to tails. Another physical process that can lead to tails in a TOF mass spectrum is
368 the time-delayed thermal desorption of a surface ion otherwise created through an athermal (e.g.
369 photoexcitation, tunneling, photoionization) process. In other words, the ionization event can be
370 athermal, but desorption may still occur through a thermal process and may not happen
371 simultaneously. The concept of ionization and desorption as discrete activities is well understood
372 for the analogous processes of electron stimulated desorption (ESD) and photon stimulated
373 desorption (PSD), and has been exhaustively verified by both modeling and experiment. The
374 models describing athermal surface ionization and subsequent desorption in ESD and PSD under
375 an applied electric field comprise those by Menzel, Gomer, and Redhead (Menzel, 1983; Menzel
376 & Gomer, 1964; Gomer, 1959; Jaeger et al., 1983; Redhead, 2011), Antoniewicz (Antoniewicz,
377 1980), and Knotek and Feibelman(Knotek & Feibelman, 1978; Knotek et al., 1979). These models
378 predict that the escape probability of a surface ion is field-dependent and has a characteristic time
379 constant. At the highest fields, ionization and desorption are instantaneous. In that case, ion
380 emission times would be on the order of the pulse width, and the resulting mass spectral peak
381 widths would be practically limited by the response of the timing electronics--there would be no
382 tails. However, at moderate fields an energy barrier to desorption of a surface ion has been
383 observed both theoretically and experimentally (Drachsel et al., 1980; Jaenicke et al., 1987;
384 Mazumder et al., 2010). Surface ion lifetimes will be longer in that case, and subsequent desorption
385 must be thermally activated (requires vibration). Desorption under moderate fields can therefore
386 be time delayed, thus leading to tails. Indeed, for strong dielectrics like SiO_2 the net surface field

may be moderate, even with a relatively high standing voltage. Other sources of tails could be delayed correlated evaporation or from secondary (impact) ionization resulting from a photoelectron shower, an Auger electron shower, or X-ray stimulated ESD (XESD) (Jaeger et al., 1983). Therefore, for peak tails observed in TOF mass spectral data, persistent heating is only one possible cause; the tails can be the result of myriad other processes. Based on the low fluence of the EUV source used here, a bulk-heating thermal process does not necessarily fit as a satisfactory explanation for the tails present in these data.

As mentioned previously, there are a handful of possible ionization and desorption mechanisms that could be operating in EUV APT. For completeness, note that ablation is not possible in these experiments as the fluence in the APT experiments is many orders of magnitude less than is typically used for ablation studies (Heinbuch et al., 2008; Kuznetsov et al., 2015). The fixed experimental conditions in this initial configuration (pulse energy, repetition rate) do not allow for a complete mechanistic understanding of the physics underlying EUV radiation-triggered ionization at this time.

The photon energy alone is sufficient to cause direct ionization of the constituent atoms. The evaporation rate and signal-to-noise ratio are effectively independent of the base temperature, and significantly, the potential maximum *bulk* temperature rise calculated from conservative conservation of energy arguments is negligible. The classic picture of a bulk heating and cooling mechanism, as seen in NUV APT, does not appear to be possible. However, if fast electron-phonon decay is localized very close to the absorption site, and heating is confined to a very small volume at the surface, then temperatures may begin to approach those required for field evaporation.

Together these facts suggest that it is reasonable to consider that a different ionization and desorption pathway may be operative in EUV compared to NUV APT for SiO_2. Future work will be aimed at determining the mechanism of EUV radiation-triggered field ion emission. Materials such as MgO, which exhibit large oxygen deficiencies and sensitive temperature dependencies in NUV APT (Mancini et al., 2014), may be better candidates to more fully explore the performance and mechanism of EUV APT.

Conclusions

The data presented here unambiguously demonstrate, for the first time, that fs-pulsed coherent EUV light of 29.6 nm wavelength (41.85 eV photon energy) is capable of driving controlled field ion emission of substrate atoms as is required to perform atom probe tomography. Mass spectral data were obtained from SiO_2 specimens at four different base temperatures in the range between 25 K and 150 K. The mass spectra show sharp, well-formed peaks of ions of Si, O, Si_2, O_2, SiO, and SiO_2. The measured compositions do not show a significant deviation from the expected stoichiometry, and show no clear trend with base temperature nor evaporation rate. That near stoichiometric measurements were achieved under all explored conditions, even with limited control of parameters, is noteworthy and suggests avenues for further exploration. Basic energy analysis of the current experimental setup indicates that the EUV radiation-assisted field ion emission is not primarily due to traditional bulk heating, however, the exact mechanism is not understood at this time and is the subject of future work.

Acknowledgements

We thank Daniel Hickstein and Jennifer Ellis for their help in the design of the EUV beamline, as well as Thomas Kelly and Marla Dowell for support of this project since its inception. We gratefully acknowledge financial support from the NIST Innovations in Measurement Science Program and material support from CAMECA Instruments through a cooperative research and development agreement.

References

ANTONIEWICZ, P. R. (1980). Model for electron- and photon-stimulated desorption. *Physical Review B* **21**, 3811–3815. https://link.aps.org/doi/10.1103/PhysRevB.21.3811 (Accessed July 2, 2019).

ARNOLDI, L., SILAEVA, E. P., GAILLARD, A., VURPILLOT, F., BLUM, I., RIGUTTI, L., DECONIHOUT, B. & VELLA, A. (2014). Energy deficit of pulsed-laser field-ionized and field-emitted ions from non-metallic nano-tips ARTICLES YOU MAY BE INTERESTED IN. *J. Appl. Phys* **115**, 203705. https://doi.org/10.1063/1.4879315 (Accessed July 23, 2019).

BACHHAV, M., DANOIX, F., HANNOYER, B., BASSAT, J. M. & DANOIX, R. (2013). Investigation of O-18 enriched hematite (α-Fe2O3) by laser assisted atom probe tomography. *International Journal of Mass Spectrometry* **335**, 57–60. https://www.sciencedirect.com/science/article/pii/S138738061200379X (Accessed June 28, 2019).

BERTHOLD, J. W., JACOBS, S. F. & NORTON, M. A. (1977). Dimensional stability of fused silica, invar, and several ultra-low thermal expansion materials. *Metrologia* **13**, 9–16.

BLANCHARD, P., CHIARAMONTI, A. N., SANFORD, N. A. & BARILI, S. (2018). An Open-Source, Graphical Software Package for Computer-Assisted Species Assignment in Atom Probe Tomography Compositional Analysis. In *APT&M 2018 Atom Probe Tomography and Microscopy*, International Field Emission Society (Ed.), p. 316. Gaithersburg, MD: NIST https://www.nist.gov/sites/default/files/documents/2018/05/29/aptm_draft_7.pdf.

BLUM, I., ZANUTTINI, D., RIGUTTI, L., VURPILLOT, F., DOUADY, J., JACQUET, E., ANGLADE, P.-M., GERVAIS, B., VELLA, A. & GAILLARD, A. (2016). Dissociation of Molecular Ions During the DC Field Evaporation ZnO in Atom Probe Tomography. *Microscopy and*

Microanalysis **22**, 662–663. http://www.journals.cambridge.org/abstract_S1431927616004165 (Accessed October 15, 2019).

BUNTON, J. H., OLSON, J. D., LENZ, D. R. & KELLY, T. F. (2007). Advances in Pulsed-Laser Atom Probe: Instrument and Specimen Design for Optimum Performance. *Microscopy and Microanalysis* **13**, 418–427. https://www.cambridge.org/core/product/identifier/S1431927607070869/type/journal_article (Accessed June 27, 2019).

BUNTON, J., OLSON, J., LENZ, D., LARSON, D. & KELLY, T. (2010). Optimized Laser Thermal Pulsing of Atom Probe Tomography: LEAP 4000X™. *Microscopy and Microanalysis* **16**, 10–11. https://www.cambridge.org/core/product/identifier/S1431927610060241/type/journal_article (Accessed June 27, 2019).

CARINI, GIOVANNI, CARINI, GIUSEPPE, COSIO, D., D'ANGELO, G. & ROSSI, F. (2016). Low temperature heat capacity of permanently densified SiO_2 glasses. *Philosophical Magazine* **96**, 761–773. https://www.tandfonline.com/doi/full/10.1080/14786435.2015.1122845 (Accessed January 27, 2020).

CEREZO, A., SMITH, G. D. W. & CLIFTON, P. H. (2006). Measurement of temperature rises in the femtosecond laser pulsed three-dimensional atom probe. *Applied Physics Letters* **88**, 154103. http://aip.scitation.org/doi/10.1063/1.2191412 (Accessed June 27, 2019).

CEREZO, A., SMITH, G. D. W. & WAUGH, A. R. (1984). THE FIM100 - PERFORMANCE OF A COMMERCIAL ATOM PROBE SYSTEM. *Le Journal de Physique Colloques* **45**, C9-329-C9-335. http://www.edpsciences.org/10.1051/jphyscol:1984955 (Accessed June 27, 2019).

CHEN, Y. M., OHKUBO, T. & HONO, K. (2011). Laser assisted field evaporation of oxides in atom probe analysis. *Ultramicroscopy* **111**, 562–566. https://www.sciencedirect.com/science/article/pii/S0304399110003554 (Accessed June 27, 2019).

CHIARAMONTI, A. N., MIAJA-AVILA, L., BLANCHARD, P. T., DIERCKS, D. R., GORMAN, B. P. & SANFORD, N. A. (2019). A Three-Dimensional Atom Probe Microscope Incorporating a Wavelength-Tuneable Femtosecond-Pulsed Coherent Extreme Ultraviolet Light Source. *MRS Advances* 1–9. https://www.cambridge.org/core/product/identifier/S2059852119002962/type/journal_article (Accessed July 9, 2019).

DECONIHOUT, B., VURPILLOT, F., GAULT, B., DA COSTA, G., BOUET, M. & BOSTEL, A. (2004). Toward a LaWaTAP: Laser assisted wide angle tomographic atom probe. In *49th International Field Emission Symposium*, pp. 278–282. Seggau Castle, Austria: John Wiley & Sons, Ltd.

DECONIHOUT, B., VURPILLOT, F., GAULT, B., DA COSTA, G., BOUET, M., BOSTEL, A., BLAVETTE, D., HIDEUR, A., MARTEL, G. & BRUNEL, M. (2007). Toward a laser assisted wide-angle tomographic atom-probe. In *Surface and Interface Analysis*vol. 39, pp. 278–282. John Wiley & Sons, Ltd http://doi.wiley.com/10.1002/sia.2491 (Accessed June 27, 2019).

DIERCKS, D. R. & GORMAN, B. P. (2016). Experimental Evaluation of the Interrelationships Between Laser Energy, Temperature, Applied Bias, and Measured Composition in Laser Pulsed Atom Probe Tomography. *Microscopy and Microanalysis* **22**, 648–649. http://www.journals.cambridge.org/abstract_S1431927616004098 (Accessed September 5, 2019).

DRACHSEL, W., JAENICKE, S., CISZEWSKI, A., DOSSELMANN, J. & BLOCK, J. (1987). Photon stimulated field desorption of hydrogen from rhodium. *Journal de Physique Colloques* **48**, C6-227.

DRACHSEL, W., NISHIGAKI, S. & BLOCK, J. H. (1980). Photon-induced field ionization mass spectroscopy. *International Journal of Mass Spectrometry and Ion Physics* **32**, 333–343. https://www.sciencedirect.com/science/article/pii/0020738180800179 (Accessed October 15, 2019).

DRACHSEL, W., WEIGMANN, W., JAENICKE, S. & BLOCK, J. H. (1985). Photon-induced field desorption experiments with laser and synchrotron radiation. In *Desorption induced by electronic transitions DIETII: Proceedings of the second international workshop, Schlob Elmau, Bavaria, October 15-17, 1984*, Brenig, W. & Menzel, D. (Eds.), p. 245. Berlin: Springer-Verlag.

DUGUAY, S., NGAMO, M., FAZZINI, P. F., CRISTIANO, F., DAOUD, K. & PAREIGE, P. (2010). Atomic scale study of a MOS structure with an ultra-low energy boron-implanted silicon substrate. *Thin Solid Films* **518**, 2398–2401. https://www.sciencedirect.com/science/article/pii/S0040609009016307 (Accessed June 28, 2019).

EERNISSE, E. P. (1974). Compaction of ion-implanted fused silica ARTICLES YOU MAY BE INTERESTED IN. *Journal of Applied Physics* **45**, 167. https://doi.org/10.1063/1.1662952 (Accessed January 27, 2020).

ERNST, N. & BLOCK, J. H. (1983). Temperature programmed field desorption of protonated hydrogen from rhodium and tungsten. *Surface Science* **126**, 397–404. https://linkinghub.elsevier.com/retrieve/pii/0039602883907343 (Accessed October 15,

2019).

GAULT, B., CHEN, Y. M., MOODY, M. P., OHKUBO, T., HONO, K. & RINGER, S. P. (2011). Influence of the wavelength on the spatial resolution of pulsed-laser atom probe. *Journal of Applied Physics* **110**, 094901. http://aip.scitation.org/doi/10.1063/1.3657846 (Accessed October 15, 2019).

GAULT, B., MOODY, M. P., CAIRNEY, J. M. & RINGER, S. P. (2012). *Atom Probe Microscopy*. New York, NY: Springer New York http://link.springer.com/10.1007/978-1-4614-3436-8 (Accessed June 27, 2019).

GAULT, B., SAXEY, D. W., ASHTON, M. W., SINNOTT, S. B., CHIARAMONTI, A. N., MOODY, M. P. & SCHREIBER, D. K. (2016). Behavior of molecules and molecular ions near a field emitter. *New Journal of Physics* **18**, 033031. http://stacks.iop.org/1367-2630/18/i=3/a=033031?key=crossref.4f84ef53e290391c109cefe9b4ab3052 (Accessed July 1, 2019).

GAULT, B., VURPILLOT, F., VELLA, A., GILBERT, M., MENAND, A., BLAVETTE, D. & DECONIHOUT, B. (2006). Design of a femtosecond laser assisted tomographic atom probe. *Review of Scientific Instruments* **77**, 043705. http://aip.scitation.org/doi/10.1063/1.2194089 (Accessed June 27, 2019).

GIL, L., RAMOS, M. A., BRINGER, A. & BUCHENAU, U. (1993). Low-temperature specific heat and thermal conductivity of glasses. *Physical Review Letters* **70**, 182–185.

GILBERT, M., VANDERVORST, W., KOELLING, S. & KAMBHAM, A. K. (2011). Atom probe analysis of a 3D finFET with high-k metal gate. *Ultramicroscopy* **111**, 530–534. https://www.sciencedirect.com/science/article/pii/S0304399110003670 (Accessed June 28, 2019).

GIN, S., RYAN, J. V., SCHREIBER, D. K., NEEWAY, J. & CABIÉ, M. (2013). Contribution of atom-probe tomography to a better understanding of glass alteration mechanisms: Application to a nuclear glass specimen altered 25 years in a granitic environment. *Chemical Geology* **349–350**, 99–109. https://www.sciencedirect.com/science/article/pii/S0009254113001447 (Accessed July 1, 2019).

GOMER, R. (1959). Field Desorption. *J. Chem. Phys* **31**, 1613. https://doi.org/10.1063/1.1730354 (Accessed July 2, 2019).

GRUBER, M., OBERDORFER, C., STENDER, P. & SCHMITZ, G. (2009). Laser-assisted atom probe analysis of sol–gel silica layers. *Ultramicroscopy* **109**, 654–659. https://www.sciencedirect.com/science/article/pii/S0304399108003379 (Accessed June 28, 2019).

GULLIKSON, E. M. (2009). Mass Absorption Coefficients. In *X-Ray Data Booklet*, Thompson, A. C. (Ed.), pp. 1-38:1-43. Berkeley: Center for X-Ray Optics, Advanced Light Source, Lawrence Berkeley National Laboratory.

HEINBUCH, S., DONG, F., ROCCA, J. J. & BERNSTEIN, E. R. (2008). Gas-phase study of the reactivity of optical coating materials with hydrocarbons by use of a desktop-size extreme-ultraviolet laser. *Journal of the Optical Society of America B* **25**, B85. https://www.osapublishing.org/abstract.cfm?URI=josab-25-7-B85 (Accessed July 11, 2019).

HONO, K., OHKUBO, T., CHEN, Y. M., KODZUKA, M., OH-ISHI, K., SEPEHRI-AMIN, H., LIA, F., KINNO, T., TOMIYA, S. & KANITANI, Y. (2011). Broadening the applications of the atom probe technique by ultraviolet femtosecond laser. *Ultramicroscopy* **111**, 576–583. https://www.sciencedirect.com/science/article/pii/S0304399110003104 (Accessed June 27,

2019).

HOUARD, J., VELLA, A., VURPILLOT, F. & DECONIHOUT, B. (2010). Optical near-field absorption at a metal tip far from plasmonic resonance. *Physical Review B - Condensed Matter and Materials Physics* **81**. https://journals.aps.org/prb/pdf/10.1103/PhysRevB.81.125411 (Accessed June 27, 2019).

ISO-21348 (2013). *ISO-21348 Definitions of Solar Irradiance Spectral Categories*.

JAEGER, R., STOHR, J. & KENDELEWICZ, T. (1983). *Ion desorption from surfaces following photon excitation of core electrons in the bulk*. https://journals.aps.org/prb/pdf/10.1103/PhysRevB.28.1145 (Accessed July 11, 2019).

JAENICKE, S., CISZEWSKI, A., DOSSELMANN, J., DRACHSEL, W., BLOCK, J.H. & MENZEL, D. (1988). Photon-stimulated desorption in high electric fields. In *Desorption induced by electronic transitions DIETIII: Proceedings of the third international workshop, Shelter Island, New York, May 20-22, 1987*, Stulen, R. . & Knotek, M. L. (Eds.), p. 236. Berlin: Springer-Verlag.

JAENICKE, S., CISZEWSKI, A., DOSSELMANN, J., DRACHSEL, W., BLOCK, J. & MENZEL, D. (1988). Field-induced structural changes in adsorbed layers of polar molecules studied by photon-stimulated desorption. *Journal de Physique Colloques* **49**, C6-191.

JAENICKE, S., CISZEWSKI, A., DRACHSEL, W., WEIGMANN, W., TSONG, T., PITTS, J., BLOCK, J. & MENZEL, D. (1986). Field-assisted photodesorption of ions from metal and semiconductor surfaces. *Journal de Physique Colloques* **47**, C7-343.

JAENICKE, S., WEIGMANN, W., PITTS, J. R., DRACHSEL, W., BLOCK, J. H. & MENZEL, D. (1987). Field-assisted photodesorption of He, Ne, Ar, Kr, and CO ions from W. *Chemical Physics* **115**, 381–389.

JOHNSON, L. J. S., THUVANDER, M., STILLER, K., ODÉN, M. & HULTMAN, L. (2013). Blind deconvolution of time-of-flight mass spectra from atom probe tomography. *Ultramicroscopy* **132**, 60–64. https://www.sciencedirect.com/science/article/pii/S0304399113000855 (Accessed June 28, 2019).

KELLOGG, G. L. (1982). Field ion microscopy and pulsed laser atom-probe mass spectroscopy of insulating glasses ARTICLES YOU MAY BE INTERESTED IN. *Journal of Applied Physics* **53**, 6383. https://doi.org/10.1063/1.33150953,6383 (Accessed June 28, 2019).

———— (1987). Pulsed-laser atom probe mass spectroscopy. *J. Phys. E: Sci. Instrum* **20**. https://iopscience.iop.org/article/10.1088/0022-3735/20/2/002/pdf (Accessed June 27, 2019).

KELLOGG, G. L. & TSONG, T. T. (1980). Pulsed-laser atom-probe field-ion microscopy. *Journal of Applied Physics* **51**, 1184–1193. http://aip.scitation.org/doi/10.1063/1.327686 (Accessed June 27, 2019).

KELLY, T. F. & MILLER, M. K. (2007). Invited review article: Atom probe tomography. *Review of Scientific Instruments* **78**, 031101.

KELLY, T. F., VELLA, A., BUNTON, J. H., HOUARD, J., SILAEVA, E. P., BOGDANOWICZ, J. & VANDERVORST, W. (2014). Laser pulsing of field evaporation in atom probe tomography. *Current Opinion in Solid State and Materials Science* **18**, 81–89. https://www.sciencedirect.com/science/article/pii/S1359028613000983 (Accessed June 27, 2019).

KINNO, T., TOMITA, M., OHKUBO, T., TAKENO, S. & HONO, K. (2014). Laser-assisted atom probe tomography of 18O-enriched oxide thin film for quantitative analysis of oxygen. *Applied*

Surface Science **290**, 194–198. https://www.sciencedirect.com/science/article/pii/S016943321302117X (Accessed June 28, 2019).

KNOTEK, M. L. & FEIBELMAN, P. J. (1978). Ion desorption by core-hole Auger decay. *Physical Review Letters* **40**, 964–967.

KNOTEK, M. L., JONES, V. O. & REHM, V. (1979). Photon-stimulated desorption of ions. *Physical Review Letters* **43**, 300–303.

KUZNETSOV, I., FILEVICH, J., DONG, F., WOOLSTON, M., CHAO, W., ANDERSON, E. H., BERNSTEIN, E., CRICK, D. C., ROCCA, J. J. & MENONI, C. S. (2015). Three-dimensional nanoscale molecular imaging by extreme ultraviolet laser ablation mass spectrometry. *Nature Communications* **6**, 6944.

KWAK, C.-M., SEOL, J.-B., KIM, Y.-T. & PARK, C.-G. (2017). Laser-assisted atom probe tomography of four paired poly-Si/SiO2 multiple-stacks with each thickness of 10 nm. *Applied Surface Science* **396**, 497–503. https://www.sciencedirect.com/science/article/pii/S0169433216323194 (Accessed June 28, 2019).

LAIGINHAS, F. A., PEREZ-HUERTA, A., MARTENS, R. L., PROSA, T. J. & REINHARD, D. (2015). Atom Probe Tomography Analysis of Bulk Chemistry in Mineral Standards. *Microscopy and Microanalysis* **21**, 843–844. http://www.journals.cambridge.org/abstract_S1431927615005012 (Accessed June 28, 2019).

LARSON, D., ALVIS, R., LAWRENCE, D., PROSA, T., ULFIG, R., REINHARD, D., CLIFTON, P., GERSTL, S., BUNTON, J., LENZ, D., KELLY, T. & STILLER, K. (2008). Analysis of Bulk

Dielectrics with Atom Probe Tomography. *Microscopy and Microanalysis* **14**, 1254–1255. https://www.cambridge.org/core/product/identifier/S1431927608083657/type/journal_article (Accessed June 28, 2019).

LARSON, D. J., PROSA, T. J., ULFIG, R. M., GEISER, B. P. & KELLY, T. F. (2013). *Local Electrode Atom Probe Tomography*. New York, NY: Springer New York http://link.springer.com/10.1007/978-1-4614-8721-0 (Accessed June 27, 2019).

LEFEBVRE-ULRIKSON, W., VURPILLOT, F. & SAUVAGE, X. (2016). *Atom probe tomography : put theory into practice*. Academic Press.

LICHTMAN, D. & SHAPIRA, Y. (1978). Photodesorption: A critical review. *Critical Reviews in Solid State and Materials Sciences* **8**, 93–118. http://www.tandfonline.com/doi/abs/10.1080/10408437808243619 (Accessed June 27, 2019).

MANCINI, L., AMIRIFAR, N., SHINDE, D., BLUM, I., GILBERT, M., VELLA, A., VURPILLOT, F., LEFEBVRE, W., LARDÉ, R., TALBOT, E., PAREIGE, P., PORTIER, X., ZIANI, A., DAVESNNE, C., DURAND, C., EYMERY, J., BUTTÉ, R., CARLIN, J. F., GRANDJEAN, N. & RIGUTTI, L. (2014). Composition of wide bandgap semiconductor materials and nanostructures measured by atom probe tomography and its dependence on the surface electric field. *Journal of Physical Chemistry C* **118**, 24136–24151. https://hal.archives-ouvertes.fr/hal-01163403 (Accessed October 23, 2019).

MARQUIS, E. A., YAHYA, N. A., LARSON, D. J., MILLER, M. K. & TODD, R. I. (2010). Probing the improbable: imaging C atoms in alumina. *Materials Today* **13**, 34–36. https://www.sciencedirect.com/science/article/pii/S136970211070184X (Accessed July 1, 2019).

MAZUMDER, B., VELLA, A., GILBERT, M., DECONIHOUT, B. & SCHMITZ, G. (2010). Reneutralization time of surface silicon ions on a field emitter. *New Journal of Physics* **12**, 113029. http://stacks.iop.org/1367-2630/12/i=11/a=113029?key=crossref.28a08240173ab8f74daae04f0b0cec3e (Accessed July 1, 2019).

MENAND, A. & KINGHAM, D. R. (1985). Evidence for the quantum mechanical tunneling of boron ions. *J. Phys. C: Solid State Phys.* **18**, 4539.

MENAND, A., MARTIN, C. & SARRAU, J. M. (1984). Field evaporation charge state of boron ions: A temperature effect study. *Journal de Physique Colloques* **45**, C9-95. https://hal.archives-ouvertes.fr/jpa-00224395 (Accessed July 9, 2019).

MENZEL, D. (1983). Mechanisms of electronically induced desorption of ions and neutrals. In *Desorption induced by electronic transitions DIETI: Proceedings of the first international workshop, Williamsburg, VA, USA, May 12-14, 1982*, Tolk, N. H., Traum, M. M., Tully, J. C. & Madey, T. E. (Eds.), p. 53. Berlin: Springer-Verlag.

MENZEL, D. & GOMER, R. (1964). Desorption from Metal Surfaces by Low-Energy Electrons. *The Journal of Chemical Physics* **41**, 3311–3328. http://aip.scitation.org/doi/10.1063/1.1725730 (Accessed July 2, 2019).

MIAJA-AVILA, L., LEI, C., AESCHLIMANN, M., GLAND, J. L., MURNANE, M. M., KAPTEYN, H. C. & SAATHOFF, G. (2006). Laser-Assisted Photoelectric Effect from Surfaces. *Physical Review Letters* **97**, 113604. https://link.aps.org/doi/10.1103/PhysRevLett.97.113604 (Accessed July 9, 2019).

MILLER, M. K. & FORBES, R. G. (2014). *Atom-Probe Tomography*. Boston, MA: Springer US http://link.springer.com/10.1007/978-1-4899-7430-3 (Accessed June 27, 2019).

MILLER, M. K., KELLY, T. F., RAJAN, K. & RINGER, S. P. (2012). The future of atom probe tomography. *Materials Today* **15**, 158–165. https://www.sciencedirect.com/science/article/pii/S136970211270069X (Accessed July 9, 2019).

MILLER, M. K., RUSSELL, K. F., THOMPSON, K., ALVIS, R. & LARSON, D. J. (2007). Review of Atom Probe FIB-Based Specimen Preparation Methods. *Microscopy and Microanalysis* **13**, 428–436. https://www.cambridge.org/core/product/identifier/S1431927607070845/type/journal_article (Accessed August 22, 2019).

NISHIGAKI, S., DRACHSEL, W. & BLOCK, J. H. (1979). Photon-induced field ionization mass spectrometry of ethylene on silver. *Surface Science* **87**, 389–409. https://www.sciencedirect.com/science/article/pii/0039602879905375 (Accessed July 9, 2019).

OHKUBO, T., CHEN, Y. M., KODZUKA, M., LI, F., OH-ISHI, K. & HONO, K. (2009). Laser-Assisted Atom Probe Analysis of Bulk Insulating Ceramics. *MRS Proceedings* **1231**, 1231-NN02-09. https://www.cambridge.org/core/product/identifier/S1946427400020467/type/journal_article (Accessed June 28, 2019).

PROSA, T. J. & LARSON, D. J. (2017). Modern Focused-Ion-Beam-Based Site-Specific Specimen Preparation for Atom Probe Tomography. *Microscopy and Microanalysis* **23**, 194–209. http://www.ncbi.nlm.nih.gov/pubmed/28162119 (Accessed August 22, 2019).

REDHEAD, P. A. (2011). Interaction of Slow Electrons With Chemisorbed Oxygen. *Canadian Journal of Physics* **42**, 886–905. http://www.nrcresearchpress.com/doi/10.1139/p64-083 (Accessed July 2, 2019).

RENAUD, L., MONSALLUT, P., BENARD, P., SALIOT, P., COSTA, G. DA, VURPILLOT, F. & DECONIHOUT, B. (2006). The New Laser assisted Wide Angle Tomographic Atom Probe. *Microscopy and Microanalysis* **12**, 1726–1727. https://www.cambridge.org/core/product/identifier/S1431927606063410/type/journal_article (Accessed June 27, 2019).

RUNDQUIST, A., DURFEE, C. G., CHANG, Z., HERNE, C., BACKUS, S., MURNANE, M. M. & KAPTEYN, H. C. (1998). Phase-matched generation of coherent soft X-rays. *Science (New York, N.Y.)* **280**, 1412–5. http://www.ncbi.nlm.nih.gov/pubmed/9603725 (Accessed July 9, 2019).

SANTHANAGOPALAN, D., SCHREIBER, D. K., PEREA, D. E., MARTENS, R. L., JANSSEN, Y., KHALIFAH, P. & MENG, Y. S. (2015). Effects of laser energy and wavelength on the analysis of LiFePO4 using laser assisted atom probe tomography. *Ultramicroscopy* **148**, 57–66. https://www.sciencedirect.com/science/article/pii/S0304399114001752 (Accessed July 1, 2019).

SCHIRHAGL, R., RAATZ, N., MEIJER, J., MARKHAM, M., GERSTL, S. S. A. & DEGEN, C. L. (2015). Nanometer-scale isotope analysis of bulk diamond by atom probe tomography. *Diamond and Related Materials* **60**, 60–65. https://www.sciencedirect.com/science/article/pii/S0925963515300649 (Accessed June 28, 2019).

SCHLESIGER, R., OBERDORFER, C., WÜRZ, R., GREIWE, G., STENDER, P., ARTMEIER, M., PELKA, P., SPALECK, F. & SCHMITZ, G. (2010). Design of a laser-assisted tomographic atom probe at Münster University. *Review of Scientific Instruments* **81**, 043703. http://aip.scitation.org/doi/10.1063/1.3378674 (Accessed June 27, 2019).

SCHREIBER, D. K., CHIARAMONTI, A. N., GORDON, L. M. & KRUSKA, K. (2014). Applicability of post-ionization theory to laser-assisted field evaporation of magnetite. *Applied Physics Letters* **105**.

SCHREIBER, D. K., CHIARAMONTI, A. N. & KRUSKA, K. (2020). Compositional Dependencies of Ni- and Fe-oxides to Experimental Parameters in Atom Probe Tomography. In *2020 TMS Annual Meeting & Exhibition*.

SILAEVA, E. P., ARNOLDI, L., KARAHKA, M. L., DECONIHOUT, B., MENAND, A., KREUZER, H. J. & VELLA, A. (2014). Do Dielectric Nanostructures Turn Metallic in High-Electric dc Fields? *Nano Letters* **14**, 6066–6072. http://pubs.acs.org/doi/10.1021/nl502715s (Accessed July 1, 2019).

SILAEVA, E. P., KARAHKA, M. & KREUZER, H. J. (2013). Atom Probe Tomography and field evaporation of insulators and semiconductors: Theoretical issues. *Current Opinion in Solid State and Materials Science* **17**, 211–216. https://www.sciencedirect.com/science/article/pii/S1359028613000685 (Accessed June 27, 2019).

STENDER, P., OBERDORFER, C., ARTMEIER, M., PELKA, P., SPALECK, F. & SCHMITZ, G. (2007). New tomographic atom probe at University of Muenster, Germany. *Ultramicroscopy* **107**, 726–733. https://www.sciencedirect.com/science/article/pii/S0304399107000484 (Accessed June 27, 2019).

STILLER, K., VISKARI, L., SUNDELL, G., LIU, F., THUVANDER, M., ANDRÉN, H.-O., LARSON, D. J., PROSA, T. & REINHARD, D. (2013). Atom Probe Tomography of Oxide Scales. *Oxidation of Metals* **79**, 227–238. http://link.springer.com/10.1007/s11085-012-9330-6 (Accessed June 28, 2019).

TALBOT, E., LARDÉ, R., PAREIGE, P., KHOMENKOVA, L., HIJAZI, K. & GOURBILLEAU, F. (2013). Nanoscale evidence of erbium clustering in Er-doped silicon-rich silica. *Nanoscale research letters* **8**, 39. http://www.ncbi.nlm.nih.gov/pubmed/23336324 (Accessed June 28, 2019).

TAYLOR, B. N. & KUYATT, C. E. (1994). *NIST Guidelines for Evaluating and Expressing the Uncertainty of NIST Measurement Results: NIST Technical Note 1297*.

THOMPSON, K., LAWRENCE, D., LARSON, D. J., OLSON, J. D., KELLY, T. F. & GORMAN, B. (2007). In situ site-specific specimen preparation for atom probe tomography. *Ultramicroscopy* **107**, 131–139. https://www.sciencedirect.com/science/article/pii/S0304399106001203?via%3Dihub (Accessed July 9, 2019).

TSONG, T. T. (1978). Field ion image formation. *Surface Science* **70**, 211–233. https://linkinghub.elsevier.com/retrieve/pii/0039602878904107 (Accessed July 9, 2019).

TSONG, T. T. (1984). Pulsed-laser-stimulated field ion emission from metal and semiconductor surfaces: A time-of-flight study of the formation of atomic, molecular, and cluster ions. *Physical Review B* **30**, 4946–4961. https://link.aps.org/doi/10.1103/PhysRevB.30.4946 (Accessed July 9, 2019).

TSONG, T. T., BLOCK, J. H., NAGASAKA, M. & VISWANATHAN, B. (1976). Photon stimulated field ionization. *The Journal of Chemical Physics* **65**, 2469–2470. http://aip.scitation.org/doi/10.1063/1.433338 (Accessed June 27, 2019).

TSONG, T. T. & KINKUS, T. J. (1984). Energy distributions of pulsed-laser field-desorbed gaseous ions and field-evaporated metal ions: A direct time-of-flight measurement. *Physical Review B* **29**, 529–542. https://link.aps.org/doi/10.1103/PhysRevB.29.529 (Accessed July 9, 2019).

TSONG, T. T., KINKUS, T. J. & MCLANE, S. B. (1983). Pulsed-laser stimulated field desorption of

gas molecules and field evaporation of metal atoms. *The Journal of Chemical Physics* **78**, 7497–7498.

TSONG, T. T., LIOU, Y. & MCLANE, S. B. (1984). Methods for a precision measurement of ionic masses and appearance energies using the pulsed-laser time-of-flight atom probe. *Review of Scientific Instruments* **55**, 1246–1254. http://aip.scitation.org/doi/10.1063/1.1137930 (Accessed July 9, 2019).

TSONG, T. T., MCLANE, S. B. & KINKUS, T. J. (1982). Pulsed-laser time-of-flight atom-probe field ion microscope. *Review of Scientific Instruments* **53**, 1442–1448. http://aip.scitation.org/doi/10.1063/1.1137193 (Accessed June 27, 2019).

VELLA, A. (2013). On the interaction of an ultra-fast laser with a nanometric tip by laser assisted atom probe tomography: A review. *Ultramicroscopy* **132**, 5–18. https://www.sciencedirect.com/science/article/pii/S0304399113001356 (Accessed June 27, 2019).

VELLA, A., MAZUMDER, B., DA COSTA, G. & DECONIHOUT, B. (2011). Field evaporation mechanism of bulk oxides under ultra fast laser illumination. *Journal of Applied Physics* **110**, 044321. http://aip.scitation.org/doi/10.1063/1.3610523 (Accessed June 27, 2019).

VISWANATHAN, B., DRACHSEL, W., BLOCK, J. H. & TSONG, T. T. (1979). Photon enhanced field ionization on semiconductor surfaces. *The Journal of Chemical Physics* **70**, 2582–2583. http://aip.scitation.org/doi/10.1063/1.437726 (Accessed June 27, 2019).

VURPILLOT, F., HOUARD, J., VELLA, A. & DECONIHOUT, B. (2009). Thermal response of a field emitter subjected to ultra-fast laser illumination. *Journal of Physics D: Applied Physics* **42**, 125502. http://stacks.iop.org/0022-3727/42/i=12/a=125502?key=crossref.c7c77e29026dae436f901e9d1997c8bb (Accessed

June 27, 2019).

WEIGMANN, W., DRACHSEL, W., JAENICKE, S. & BLOCK, J. H. (1984). Field ionization and field desorption stimulated by synchrotron radiation. *Journal de Physique Colloques* **45**, C9-105.

WEIGMANN, W., JAENICKE, S., PITTS, J., DRACHSEL, W. & BLOCK, J. H. (1986). Photon induced field desorption of hydrogen and noble gasses from tungsten. *Journal de Physique Colloques* **47**, C2-145.

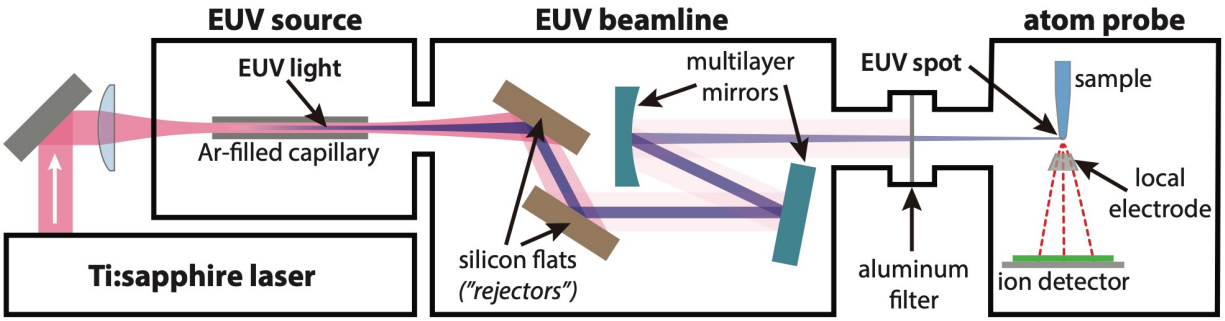

Figure 1: Schematic drawing of the EUV APT instrument. The Ti:sapphire driving laser outputs 800 nm, 35 fs pulses at a repetition rate of 10 kHz. These pulses are coaxially focused into an Ar-filled hollow capillary waveguide and coherent EUV photons are generated by means of high harmonic generation. The resulting EUV pulse width is less than 10 fs. The 800 nm driving laser and EUV light co-propagate out of the capillary waveguide into a vacuum manifold beamline. The beamline contains two reflective optics ("rejectors") that efficiently absorb the 800 nm fundamental driving laser light while reflecting a significant fraction of the EUV light. The beamline also contains the multilayer mirror optics, which pass the 27th harmonic of the fundamental (41.85 eV; 29.6 nm) with a bandwidth of ≈ 2.4 eV. These mirrors are also used to focus and steer the beam. A 200 nm thick Al filter placed just outside of the atom probe chamber removes residual driving laser light while transmitting a high fraction of the EUV wavelength. The pulse energy of the remaining EUV light was measured to be 0.5 pJ just before the beam enters the atom probe analysis chamber.

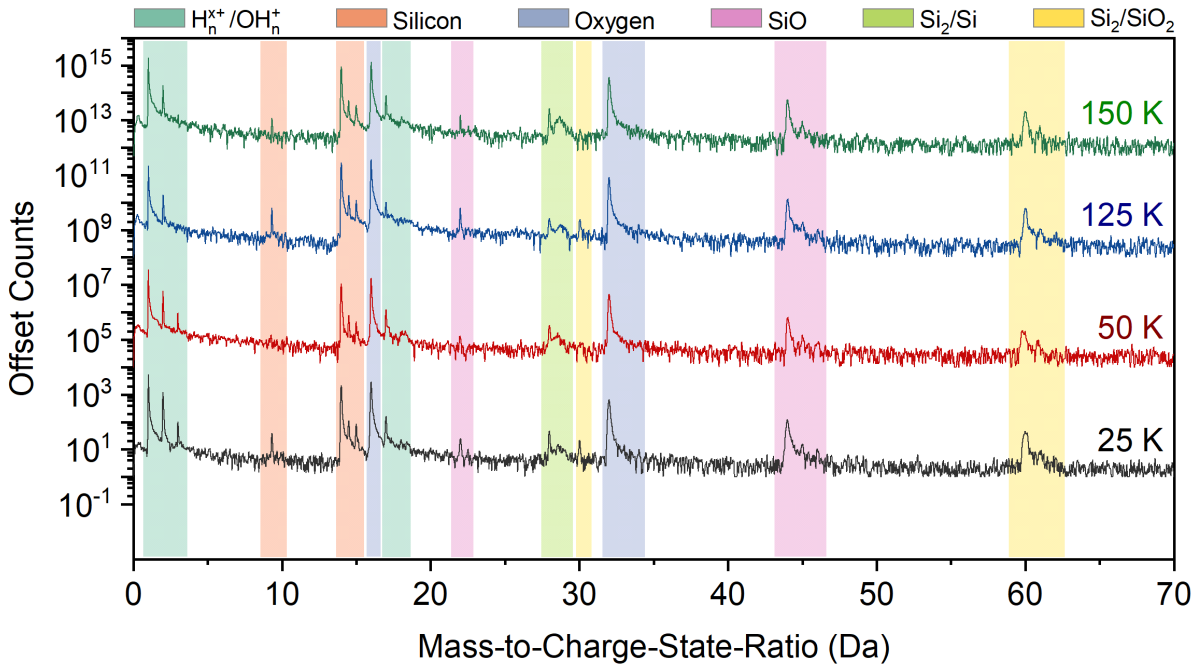

Figure 2: EUV radiation-triggered mass spectra of amorphous SiO_2 as a function of the base (standing) temperature in the range between 25 K and 150 K. The ranges corresponding to H_n^{x+}/OH_n^+ species (dark green), silicon (orange), oxygen (blue), SiO (purple), Si/Si_2 (light green), and SiO_2/Si_2 (yellow) for various charge states are indicated. The EUV atom probe microscope operates at fixed acquisition conditions of 0.5 pJ pulse energy, 41.85 eV photon energy, and a repetition rate of 10 kHz. To facilitate equal comparison, each spectrum was generated from 10^5 events. These data have not been background corrected. The display bin size is 0.03 Da.

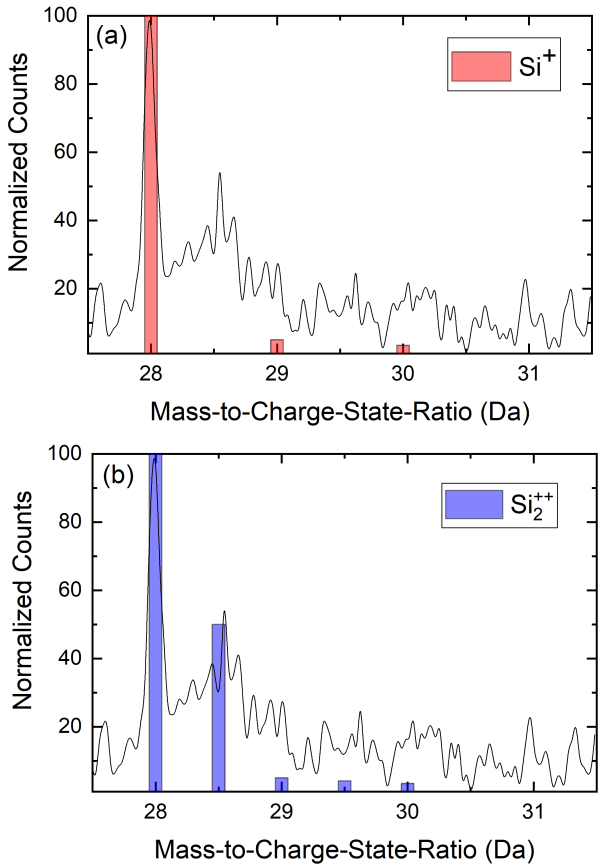

Figure 3: Subset of the 50 K mass spectrum in the range 27.5 Da to 31.5 Da, normalized to the height of the peak at 28 Da. Overlaid on the mass spectrum are graphical representations of the expected natural Si isotopic abundances for Si^{+} and Si_2^{++} ions. The peaks in this region do not fit the expected isotopic profile of either (a) Si^{+} or (b) Si_2^{++} alone. Therefore, they likely contain fractional contributions from both species (as well as their related hydrides). Peak decomposition did not provide statistically significant results due to the low number of counts in that region. Therefore, two different peak range assignments were used to bracket the range of possible compositions that the data can support: one maximally oxygen rich, and one maximally oxygen deficient. The true measured composition will necessarily lie within those bounds and could be determined more accurately given a spectrum with sufficiently high counts.

Table 1: Details of the data collection parameters for the four datasets discussed here. Two different specimens were examined at two different ion detection rates.

Base Temperature	**Analytical Chamber Pressure Torr**	**Specimen: Order of Data Collection**	**Ion Detection Rate (ions per 10^3 pulses)**	**Standing Voltage**	**Multiple Counts %**
25 K	5.2E-11	A:1	1.5	5.9 kV	22
50 K	6.4E -11	B:1	0.4	4.3 kV	17
125 K	9.7E -11	B:2	0.5	5.0 kV	23
150 K	1.2E -10	A:2	1.5	6.0 kV	18

Table 2: Mass spectrum peak assignments in order to obtain the widest range of possible of oxygen concentration that the data could possibly support. Hydrogen is not usually included when calculating bulk composition in APT; here, we are only concerned with only Si and O but the hydrides are identified for completeness. The peaks at 17 and 18 Da are expected to come primarily from the chamber and were not used in the calculation of composition.

	1 Da to 3 Da	**9 Da**	**14 Da**	**16 Da**	**17 Da, 18 Da**	**22 Da**	**28 Da to 29 Da**	**30 Da**	**32 Da**	**44 Da**	**60 Da**
Peak Assignment: Oxygen-Rich	H_n^{x+}	Si^{+++}	Si^{++}	O^{+}	OH_n^{x+}	SiO^{++}	Si^{+}	SiO_2^{++}	O_2^{+}	SiO^{+}	SiO_2+
Peak Assignment: Oxygen-Deficient	H_n^{x+}	Si^{+++}	Si^{++}	O^{+}	OH_n^{x+}	SiO^{++}	$Si_2H_n^{++}$	$Si_2H_n^{++}$	O_2^{+}	SiO^{+}	Si_2H_n+

Table 3: Measured composition as a function of the specimen base temperature and peak ranging mode. There is no obvious trend in the measured composition with the base temperature. Therefore, the average measured composition and sample standard deviation is listed for each model.

Base Temperature	**Oxygen-Rich Model Composition (at. %)**	**2σ Error (at. %)**	**Oxygen-Deficient Model Composition, (at. %)**	**2σ Error (at. %)**
25 K	X_O = 68.0, X_{Si} = 32.0	0.6	X_O = 64.4, X_{Si} 35.6	0.7
50 K	X_O = 70.7, X_{Si} 29.3	0.9	X_O = 67.3, X_{Si} 32.7	1.0
125 K	X_O = 65.8, X_{Si} 34.2	0.6	X_O = 62.6, X_{Si} 37.4	0.7
150 K	X_O = 69.3, X_{Si} 30.7	0.7	X_O = 65.6, X_{Si} 34.4	0.8
	Oxygen-Rich Model Average (at. %)	**s (at. %)**	**Oxygen-Deficient Model Average (at. %)**	**s (at. %)**
Oxygen Concentration	X_O = 68.5	2.1	X_O = 65.0	2.0

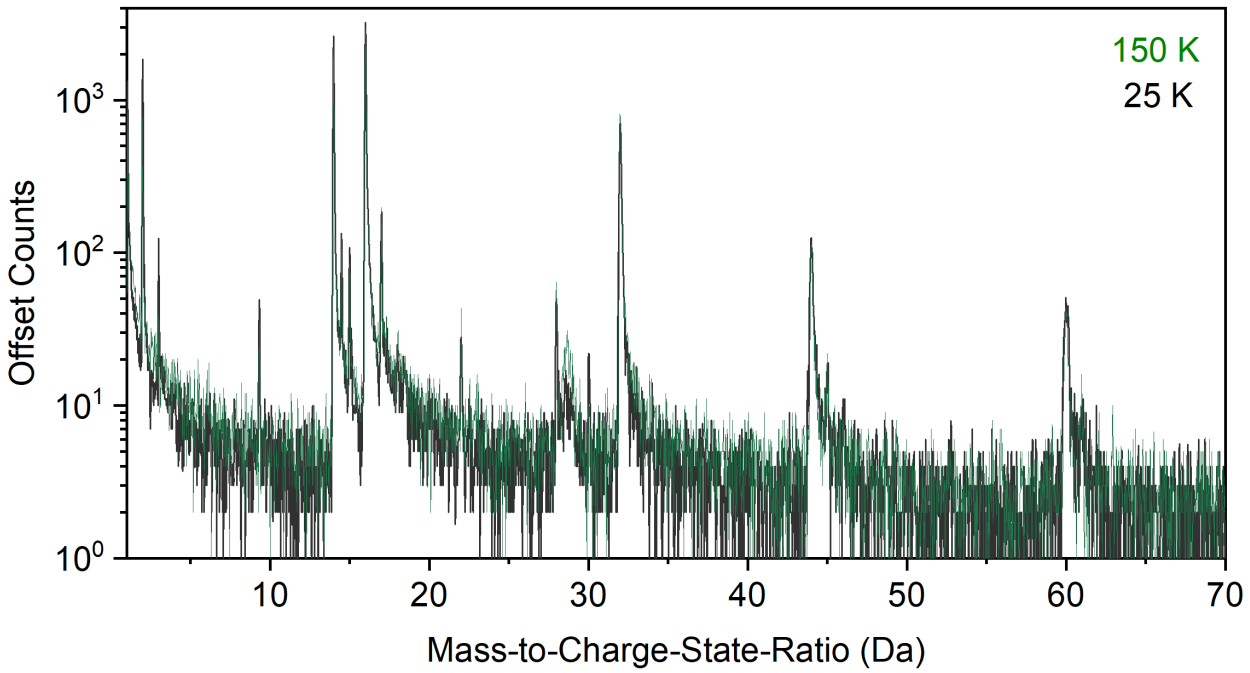

Figure S1: Mass spectra at base temperatures of 25 K and 150 K overlaid to demonstrate that the time-independent background signal is independent of the specimen base temperature for these data. If the primary source of time-independent background signal was either field evaporation or field ionization of adsorbed, field adsorbed, or residual chamber gasses, one would expect to see a temperature-dependence since these processes are thermally activated and the base pressure varies by nearly an order of magnitude between 25 K and 150 K.